Acta Cryst B
STRUCTURAL SCIENCE
CRYSTAL ENGINEERING
MATERIALS

ISSN 2052-5206

Seed layer formation by deposition of microcrystallites on a revolving substrate: modeling of the effective linear elastic, piezoelectric, and dielectric coefficients

Arthur Ballato[a]* and John Ballato[b]*

[a]Holcombe Department of Electrical and Computer Engineering, Clemson University, Clemson, SC 29634, USA, and [b]Department of Materials Science and Engineering, Clemson University, Clemson, SC 29634, USA. *Correspondence e-mail: art.ballato@gmail.com, jballat@clemson.edu

Received 30 August 2024
Accepted 28 October 2024

Edited by R. Černý, University of Geneva, Switzerland

Keywords: deposition; sputtering; rotating substrate; crystallites; dielectric permittivity; piezoelectricity; elasticity; zinc oxide; engineered polycrystals; seed layers; texture.

Averaging of material coefficients of crystallites deposited at an angle to a rotating substrate is considered. A simple model is proposed, and applied to determine effective linear dielectric, piezoelectric, and elastic constants of all Laue groups. While these represent tensors of rank 2, 3, and 4, the method applies generally to tensors of any rank. Results are then particularized for 6*mm* point symmetry crystals, and applied numerically to zinc oxide, ZnO. It is shown that, by means of the rotating substrate method, depositions may be achieved having the equivalent of hexagonal anisotropy, enabling the creation of 'engineered' structures.

1. Introduction

Deposition technology is critical in micro- and nano-electronic fabrication of sensors, transducers, filters, energy harvesters, resonators, *etc*. (Martin, 2010; Behrisch, 2013*a*, Behrisch, 2013*b*; Bundesmann & Neumann, 2018). These devices most often consist of multi-layer structures, the reliability and functionality of which depend on the ability to create uniform and stable layer interfaces. One modality for assuring interface compatibility is an initial deposition between working layers of a thin 'seed' or buffer layer, whose material and composition are chosen to afford compatible adhesion and to provide suitable conditions for subsequent uniform working layer growth (Clement *et al.*, 2012; Noh *et al.*, 2014; Li *et al.*, 2020). This is particularly important when forming structures comprised of single, or quasi-single crystal piezoelectric working layers. The axial orientation of these, with respect to the substrate normal, *i.e.* the texture (Bunge, 1982; Suwas & Gurao, 2008) allows their effective piezo-coupling and elastic values to be optimized (Bjurström *et al.*, 2006; Yanagitani *et al.*, 2007*a*; Du *et al.*, 2009; Moreria *et al.*, 2011).

It is found that often superior seed layers are achieved by deposition of microcrystallites at a single angle to a revolving substrate (Stedile *et al.*, 1994; Auger *et al.*, 2002; Mertin *et al.*, 2018). The substrate rotation averages the crystallite properties, resulting in a polycrystalline aggregate film with material properties modified from the single crystal values of the seed material. After deposition of the seed layer, the substrate rotation is halted, and deposition of the textured film is commenced. This oriented film may be of the same material as that of the seed, or may, indeed, be of any material, deposited at the same angle as that of the seed microcrystals, or at any

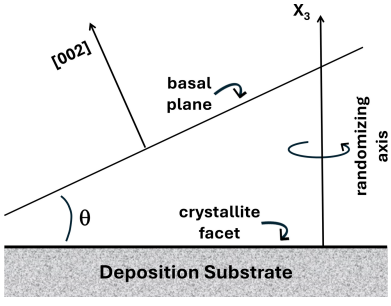

desired angle. This is arranged by suitable adjustment of the deposition apparatus parameters.

This work derives effective values for the elastic stiffnesses, piezoelectric stress coefficients, and dielectric permittivities of the seed layer using a simple model outlined below. The model may easily be expanded to accommodate a more realistic orientation distribution function characterizing the incident seed layer flux, rather than a fixed single deposition angle. It is noted that material values deviate from those of the bulk as crystallite size diminishes; this is usual when the micro/nano-boundary is crossed. The effective crystallite material coefficients are to be substituted for those of the bulk, with no changes in the averaging procedure described herein.

If the seed layer is not constrained to be 'thin', then other potential configurations emerge. It becomes possible to construct an assortment of tailored structures such as acoustic and optical Bragg reflectors consisting of alternating high- and low-impedance layers (Newell, 1964; Link *et al.*, 2006; Dvoesherstov *et al.*, 2013), as utilized, for example, in solidly mounted resonators (Lakin, 2003; Iborra *et al.*, 2012; Nguyen *et al.*, 2019). Other options are enabled as well, such as superlattices (Schuller, 1980; Akçakaya *et al.*, 1990; Bykhovski *et al.*, 1997), including Fibonacci and Moiré designs (MacDonald, 1988; Dean *et al.*, 2013; Mouldi & Kanzari, 2013). A simple example is offered in Section 4 where ZnO microcrystals are considered to be deposited with (103) planes parallel to the revolving substrate plane. Substrate rotation, and consequent angular averaging (see Section 2), produces an engineered crystal, again with 6*mm* symmetry, albeit with modified material coefficients, which are computed.

2. The model

Microcrystallites are deposited on a revolving substrate, all with a specified facet lying in the substrate plane. The x_3 axis of the crystallite is thus inclined with respect to the substrate normal (X_3) by a facet angle θ; see Fig. 1. The substrate revolution, in angle φ, creates a distribution of crystallite normals ([002] in the diagram) that form a cone about the substrate normal. The model assumes a uniform areal distribution of crystallites on the substrate. A suitable angular averaging then yields effective values $\langle q\rangle = [1/(2\pi)]\int_0^{2\pi} q\,\mathrm{d}\varphi$, where q is the quantity to be averaged. In the following sections this averaging is carried out schematically on the point-group matrices characterizing the linear elastic, piezo, and dielectric crystal properties. These three families of phenomenological coefficients are much utilized in electroacoustic applications and are used here to illustrate the results applied to tensors of ranks 2, 3, and 4 in their matrix form. The model may be extended to material tensors of arbitrary rank.

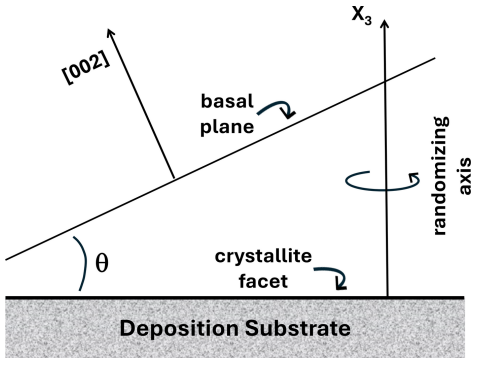

Figure 1
Schematic of the deposition geometry. The crystallite facet lies upon the substrate; its x_3 axis, shown as [002], subtends cone angle θ with respect to the substrate randomizing axis X_3.

Table 1
Averaged dielectric permittivities, $\langle\varepsilon_{kk}''\rangle$, in terms of the singly rotated quantities, ε_{ij}'.

$\langle\varepsilon_{kk}''\rangle$	Groups I–VI	Group VII
$\langle\varepsilon_{11}''\rangle$	$\frac{1}{2}(\varepsilon_{11}' + \varepsilon_{22}')$	ε_{11}'
$\langle\varepsilon_{33}''\rangle$	ε_{33}'	ε_{11}'

Axial conventions, and associated nomenclature, for the point groups are given, *e.g.* in Institute of Radio Engineers Standards Committee (1949); symmetry relations relating the tensorial material coefficients are succinctly discussed by Bhagavantam & Suryanarayana (1949), Fumi (1952*a*), Fumi (1952*b*), Fumi (1952*c*), Fieschi (1957), and in engineering format by Cady (1946), Cady (1964) Mason (1966), Nye (1985). Tensor coefficients describing the elastic, piezo, and dielectric effects, are transformed according to standard rules (Bond, 1943; Juretschke, 1952; Bechmann, 1960; Hearmon, 1957). Initially, the crystallite x_3 axis is normal to the substrate reference plane, and a first rotation about its x_1 or x_2 axis carries it to the configuration shown in Fig. 1. The elastic, piezoelectric, and dielectric matrices resulting from this first rotation are denoted $[c']$, $[e']$, and $[\varepsilon']$, respectively. Subsequent rotation of the crystallite sitting on the substrate plane is described by a second rotation about its x_3' axis; the averaging is carried out on the resulting transformed quantities, with final averaged results denoted as $\langle c''\rangle$, $\langle e''\rangle$, and $\langle\varepsilon''\rangle$.

3. Model results for all Laue groups

In this section are given the averaged components, $\langle''\rangle$, of the dielectric, piezoelectric, and elastic tensors for all Laue groups (Bechmann & Hearmon, 1969; Brendel, 1979).

3.1. Linear dielectric permittivities

Five distinct, symmetric, permittivity matrices, $[\varepsilon]$, corresponding to Laue groups I, II, III, IV–VI, and VII, characterize the linear dielectric behavior of crystals (Cady, 1946, 1964; Mason, 1966; Nye, 1985). The geometry of Fig. 1 is realized by a rotation about an in-plane x_1 or x_2 axis by facet angle θ; this transforms these to five distinct matrices $[\varepsilon']$ in standard fashion. Anticipating the final result, these $[\varepsilon']$ matrices are not given explicitly. A further rotation about the resulting x_3' axis (normal to the substrate plane), and subsequent averaging by the revolving substrate produces two distinct $\langle\varepsilon''\rangle$ matrices, the components of which are given in

Table 2
Averaged dielectric permittivities for all Laue groups, for first rotation x_1 or x_2.

C and S are cos(θ) and sin(θ), respectively, where θ is the angle of first rotation, the facet angle.

Rotation	Laue →	Group I	Group II	Group III	Groups IV–VI	Group VII
x_1	$\langle\varepsilon_{11}''\rangle$	$\frac{1}{2}(\varepsilon_{11}+\varepsilon_{22}C^2+2\varepsilon_{23}CS+\varepsilon_{33}S^2)$	$\frac{1}{2}(\varepsilon_{11}+\varepsilon_{22}C^2+\varepsilon_{33}S^2)$		$\frac{1}{2}(\varepsilon_{11}+\varepsilon_{11}C^2+\varepsilon_{33}S^2)$	ε_{11}
	$\langle\varepsilon_{33}''\rangle$	$\varepsilon_{33}C^2-2\varepsilon_{23}CS+\varepsilon_{22}S^2$	$\varepsilon_{33}C^2+\varepsilon_{22}S^2$		$\varepsilon_{33}C^2+\varepsilon_{22}S^2$	ε_{11}
x_2	$\langle\varepsilon_{11}''\rangle$	$\frac{1}{2}(\varepsilon_{22}+\varepsilon_{11}C^2-2\varepsilon_{13}CS+\varepsilon_{33}S^2)$		$\frac{1}{2}(\varepsilon_{22}+\varepsilon_{11}C^2+\varepsilon_{33}S^2)$	$\frac{1}{2}(\varepsilon_{11}+\varepsilon_{11}C^2+\varepsilon_{33}S^2)$	ε_{11}
	$\langle\varepsilon_{33}''\rangle$	$\varepsilon_{33}C^2+2\varepsilon_{13}CS+\varepsilon_{11}S^2$		$\varepsilon_{33}C^2+\varepsilon_{11}S^2$		ε_{11}

Table 3
The $\langle e''\rangle$ components of matrix $\langle A\rangle$ expressed in terms of the singly rotated e' elements.

0	0	0	$\langle e_{14}''\rangle$	$\langle e_{15}''\rangle$	0	=	0	0	0	$\frac{1}{2}(e'_{14}-e'_{25})$	$\frac{1}{2}(e'_{15}+e'_{24})$	0
0	0	0	$\langle e_{15}''\rangle$	$-\langle e_{14}''\rangle$	0		0	0	0	$\frac{1}{2}(e'_{15}+e'_{24})$	$-\frac{1}{2}(e'_{14}-e'_{25})$	0
$\langle e_{31}''\rangle$	$\langle e_{31}''\rangle$	$\langle e_{33}''\rangle$	0	0	0		$\frac{1}{2}(e'_{31}+e'_{32})$	$\frac{1}{2}(e'_{31}+e'_{32})$	e_{33}''	0	0	0

Table 4
Resulting matrix after second rotation about x_3, and subsequent averaging by the revolving substrate.

Laue →	I	II		III		IVa and VIa	IVa	IVb and VIb		IVb	Va	Vb		VIa	VIb	VIIa and VIIb
H-M →	1	2	*m*	222	*mm*2	4, 6	$\overline{4}$	422, 622	4*mm*, 6*mm*	$\overline{4}2m$	3	32	3*m*	$\overline{6}$	$\overline{6}m2$	23, $\overline{4}3m$
Rotation																
x_1	$\langle A\rangle$	$\langle A\rangle$	$\langle A\rangle$	$\langle C\rangle$	$\langle B\rangle$	$\langle A\rangle$	$\langle A\rangle$	$\langle C\rangle$	$\langle B\rangle$	$\langle C\rangle$	$\langle A\rangle$	$\langle C\rangle$	$\langle B\rangle$	$\langle A\rangle$	$\langle C\rangle$	$\langle C\rangle$
x_2	$\langle A\rangle$	$\langle C\rangle$	$\langle B\rangle$	$\langle C\rangle$	$\langle B\rangle$	$\langle A\rangle$	$\langle A\rangle$	$\langle C\rangle$	$\langle B\rangle$	$\langle C\rangle$	$\langle A\rangle$	$\langle A\rangle$	$\langle A\rangle$	$\langle A\rangle$	$\langle B\rangle$	$\langle C\rangle$

Table 5
Singly rotated e' coefficients for triclinic Laue group I in terms of the unrotated e coefficients.

With θ the angle of first rotation about x_1, C and S stand for cos(θ) and sin(θ), where θ is the facet angle.

e_{14}'	=	$e_{14}(C^2-S^2)+(e_{13}-e_{12})CS$
e_{15}'		$e_{15}C^2-e_{16}S$
e_{24}'		$(e_{24}C+e_{34}S)(C^2-S^2)-[(e_{22}C+e_{32}S)-(e_{23}C+e_{33}S)]CS$
e_{25}'		$(e_{25}C+e_{35}S)C-(e_{26}C+e_{36}S)S$
e_{31}'		$e_{31}C-e_{21}S$
e_{32}'		$(e_{32}C-e_{22}S)C^2+(e_{33}C-e_{23}S)S^2+2(e_{34}C-e_{24}S)CS$
e_{33}'		$(e_{33}C-e_{23}S)C^2+(e_{32}C-e_{22}S)S^2-2(e_{34}C-e_{24}S)CS$

Table 6
Singly rotated e' coefficients for triclinic Laue group I in terms of the unrotated e coefficients.

With θ the angle of first rotation about x_2, C and S stand for cos(θ) and sin(θ), where θ is the facet angle.

e_{14}'	=	$e_{14}C^2-e_{36}S^2+(e_{16}-e_{34})CS$
e_{15}'		$(e_{15}C-e_{35}S)(C^2-S^2)+[(e_{11}-e_{13})C+(e_{33}-e_{31})S]CS$
e_{24}'		$e_{24}C-e_{26}S$
e_{25}'		$e_{25}(C^2-S^2)+(e_{21}-e_{23})CS$
e_{31}'		$(e_{31}C+e_{11}S)C^2+(e_{33}C+e_{13}S)S^2-2(e_{35}C+e_{15}S)CS$
e_{32}'		$e_{32}C+e_{12}S$
e_{33}'		$(e_{33}C+e_{13}S)C^2+(e_{31}C+e_{11}S)S^2+2(e_{35}C+e_{15}S)CS$

terms of the components of $[\varepsilon']$ in Table 1, with $\langle\varepsilon_{22}''\rangle=\langle\varepsilon_{11}''\rangle$, and zero off-diagonal elements. In terms of the components of the original $[\varepsilon]$ matrices, the final result is given in Table 2.

3.2. Linear piezoelectric stress moduli

Sixteen distinct matrices $[e]$, characterize the linear piezoelectric behavior of the 20 piezoelectric classes (Cady, 1946, 1964; Mason, 1966; Nye, 1985). Each of the Laue groups is represented. The pairs (4, 6), (422, 622), (4*mm*, 6*mm*), and (23, $\overline{4}3m$) share the same matrices. The geometry of Fig. 1 is realized by a rotation about an in-plane x_1 or x_2 axis by facet angle θ; this transforms each of these sixteen to one of five distinct matrices $[e']$ in standard fashion. The Laue group I results for both x_1 and x_2 rotations are identical, so there are but nine distinct $[e']$ matrices. Again, anticipating the final result, these $[e']$ matrices are not given explicitly. A further rotation about the resulting x_3' axis (normal to the substrate plane), and subsequent averaging by the revolving substrate produces three distinct $\langle e''\rangle$ matrices, that we denote as $\langle A\rangle$, $\langle B\rangle$, and $\langle C\rangle$. The structure of matrix $\langle A\rangle$ is given in Table 3, where the $\langle e''\rangle$ components are expressed in terms of the $[e']$ components; it is identical in form to the matrix of the unrotated classes (4, 6). Matrix $\langle B\rangle$ is that of matrix $\langle A\rangle$ with $e_{14}''=e_{25}''=0$ and has the same structure as the matrix of the unrotated classes (4*mm*, 6*mm*). Finally, matrix $\langle C\rangle$ is that of matrix $\langle A\rangle$ with $e_{15}''=e_{24}''=e_{31}''=e_{32}''=e_{33}''=0$ and has the same structure as the matrix of the unrotated classes (422, 622). The averaged results for the twenty piezoelectric classes are given in Table 4.

The pertinent $[e']$ matrix components are given explicitly in terms of the components of the original $[e]$ matrices in Table 5 and Table 6 for Laue group I. These relations are easily specialized for the remaining Laue groups of higher symmetry.

3.3. Linear elastic stiffnesses

Nine distinct, symmetric, stiffness matrices, $[c]$, corresponding to Laue groups I, II, III, IVa, IVb, Va, Vb, VI, and VII, characterize the linear elastic behavior of crystals (Cady,

Table 7
Averaged elastic stiffnesses for Laue groups I–VII as function of the c' components.

The $\langle \mathbf{c}'' \rangle$ matrix possesses hexagonal symmetry.

$\langle c_{\lambda\mu}'' \rangle$		x_1 or x_2 rotation
$\langle c_{11}'' \rangle$		$\frac{1}{8}[3c_{11}' + 2c_{12}' + 3c_{22}' + 4c_{66}']$
$\langle c_{12}'' \rangle$		$\frac{1}{8}[c_{11}' + 6c_{12}' + c_{22}' - 4c_{66}']$
$\langle c_{13}'' \rangle$	=	$\frac{1}{2}[c_{13}' + c_{23}']$
$\langle c_{33}'' \rangle$		c_{33}'
$\langle c_{44}'' \rangle$		$\frac{1}{2}[c_{44}' + c_{55}']$
$\langle c_{66}'' \rangle$		$\frac{1}{8}[c_{11}' - 2c_{12}' + c_{22}' + 4c_{66}']$

Table 8
Transformed elastic stiffnesses for triclinic Laue group I, as function of the first rotation x_1.

Only the pertinent c', needed for insertion into Table 7, are listed. C and S are $\cos(\theta)$ and $\sin(\theta)$, respectively, where θ is the facet angle.

c_{11}'		c_{11}
c_{22}'		$c_{22}C^4 + c_{33}S^4 + 2[2(c_{24}C^2 + c_{34}S^2) + (c_{23} + 2c_{44})CS]CS$
c_{33}'		$c_{33}C^4 + c_{22}S^4 + 2[-2(c_{34}C^2 + c_{24}S^2) + (c_{23} + 2c_{44})CS]CS$
c_{44}'		$c_{44}(C^4 + S^4) + [2(c_{34} - c_{24})(C^2 - S^2) + (c_{22} + c_{33} - 2c_{23} - 2c_{44})CS]CS$
c_{55}'	=	$c_{55}C^2 - 2c_{56}CS + c_{66}S^2$
c_{66}'		$c_{66}C^2 + 2c_{56}CS + c_{55}S^2$
c_{12}'		$c_{12}C^2 + 2c_{14}CS + c_{13}S^2$
c_{13}'		$c_{13}C^2 - 2c_{14}CS + c_{12}S^2$
c_{23}'		$c_{23}(C^4 + S^4) + [2(c_{34} - c_{24})(C^2 - S^2) + (c_{22} + c_{33} - 4c_{44})CS]CS$
$(c_{44}' - c_{23}')$		$(c_{44} - c_{23})$

Table 9
Transformed elastic stiffnesses for triclinic Laue group I, as function of the first rotation x_2.

Only the pertinent c', needed for insertion into Table 7, are listed. C and S are $\cos(\theta)$ and $\sin(\theta)$, respectively, where θ is the facet angle.

c_{11}'		$c_{11}C^4 + c_{33}S^4 - 2[2(c_{15}C^2 + c_{35}S^2) - (c_{13} + 2c_{55})CS]CS$
c_{22}'		c_{22}
c_{33}'		$c_{33}C^4 + c_{11}S^4 + 2[2(c_{35}C^2 + c_{15}S^2) + (c_{13} + 2c_{55})CS]CS$
c_{44}'		$c_{44}C^2 + 2c_{46}CS + c_{66}S^2$
c_{55}'		$c_{55}(C^4 + S^4) + [2(c_{15} - c_{35})(C^2 - S^2) + (c_{11} + c_{33} - 2c_{13} - 2c_{55})CS]CS$
c_{66}'	=	$c_{66}C^2 - 2c_{46}CS + c_{44}S^2$
c_{12}'		$c_{12}C^2 - 2c_{25}CS + c_{23}S^2$
c_{13}'		$c_{13}(C^4 + S^4) + [2(c_{15} - c_{35})(C^2 - S^2) + (c_{11} + c_{33} - 4c_{55})CS]CS$
c_{23}'		$c_{23}C^2 + 2c_{25}CS + c_{12}S^2$
$(c_{55}' - c_{13}')$		$(c_{55} - c_{13})$

Table 10
Averaged permittivities (pF m^{-1}) for class 6*mm*, particularized for ZnO with facet plane (103).

$\langle \varepsilon_{11}'' \rangle$	$\frac{1}{2}(\varepsilon_{11}' + \varepsilon_{22}')$	=	$\frac{1}{2}(\varepsilon_{11} + \varepsilon_{11}C^2 + \varepsilon_{33}S^2)$	= 74.38
$\langle \varepsilon_{33}'' \rangle$	ε_{33}'		$\varepsilon_{33}C^2 + \varepsilon_{11}S^2$	= 77.03

1946; 1964; Mason, 1966; Nye, 1985). The geometry of Fig. 1 is realized by a rotation about an in-plane x_1 or x_2 axis by facet angle θ; this transforms each of these nine to matrices $[c']$ in standard fashion. A further rotation about the resulting x_3' axis, (normal to the substrate plane), and subsequent averaging by the revolving substrate produces, for all Laue groups, a single $\langle c'' \rangle$ matrix with hexagonal symmetry. The components of $\langle c'' \rangle$ are given in terms of the components of $[c']$ in Table 7. The pertinent $[c']$ matrix components are given explicitly in terms of the components of the original $[c]$ matrices in Tables 8 and 9 for Laue group I. These relations are easily specialized for the remaining Laue groups of higher symmetry.

4. Example: zinc oxide, Laue group VIb, class 6*mm*

Zinc oxide, in its 6*mm* polytype, is similar in many ways to the III-nitrides, and to polarized ceramics. Its high piezoelectric coupling has led to its use in a wide variety of acousto-electronic devices. Provided here are the effective material coefficients, and piezoelectric coupling factors, of deposited ZnO crystallites subjected to the averaging procedure described in Section 2. The 6*mm* symmetry requires isotropy in the basal plane, hence all rotations (tilts) about any axis, (*e.g.* x_1 or x_2), in the (001) plane will yield identical results. We take the first rotation about x_1 by a facet angle θ corresponding to the (103) plane (Kushibiki *et al.*, 2009); in the coordinate system of the substrate, this results in the equivalent of monoclinic symmetry. The averaging process then yields $\langle '' \rangle$ quantities but again with 6*mm* symmetry. The numerical input values are taken from Jaffe & Berlincourt (1965) and Pearton *et al.* (2005).

4.1. Dielectric permittivities

A first rotation, about x_1, results in $[\varepsilon']$ quantities as follows: $\varepsilon_{11}' = \varepsilon_{11}$; $\varepsilon_{12}' = \varepsilon_{13}' = 0$; $\varepsilon_{22}' = \varepsilon_{11}C^2 + \varepsilon_{33}S^2$; $\varepsilon_{23}' = (\varepsilon_{33} - \varepsilon_{11})CS$; and $\varepsilon_{33}' = \varepsilon_{33}C^2 + \varepsilon_{11}S^2$. The resulting $\langle \varepsilon'' \rangle$ components, taken from Table 2, and numerical values for ZnO referred to the facet plane (103), are given in Table 10.

4.2. Piezoelectric stress coefficients

A first rotation, about x_1, results in $[e']$ quantities as follows: $e_{15}' = e_{15}C$; $e_{16}' = e_{15}S$; $e_{21}' = e_{31}S$; $e_{22}' = [e_{33}S^2 + (e_{31} + 2e_{15})C^2]S$; $e_{23}' = [e_{31}S^2 + (e_{33} - 2e_{15})C^2]S$; $e_{24}' = [e_{33}S^2 - e_{31}S^2 + e_{15}(C^2 - S^2)]C$; $e_{31}' = e_{31}C$; $e_{32}' = [e_{31}C^2 - 2e_{15}S^2 + e_{33}S^2]C$; $e_{33}' = [e_{33}C^2 + 2e_{15}S^2 + e_{31}S^2]C$; and $e_{34}' = [e_{33}C^2 - e_{31}C^2 - e_{15}(C^2 - S^2)]S$. The subsequent averaging, from Table 4, results in matrix $\langle B \rangle$ symmetry, with components as follows: $\langle e_{15}'' \rangle = \langle e_{24}'' \rangle = (1/2)(e_{15}' + e_{24}') = (1/2)[2e_{15}C^2 + (e_{33} - e_{31})S^2]C$; $\langle e_{31}'' \rangle = \langle e_{32}'' \rangle = (1/2)(e_{31}' + e_{32}') = (1/2)[e_{31}(1 + C^2) + (e_{33} - 2e_{15})S^2]C$; $\langle e_{33}'' \rangle = [e_{33}C^2 + (e_{33} + 2e_{15})S^2]C$; numerical results are given in Table 11.

4.3. Elastic stiffnesses components

A first rotation, about x_1, results in the $[c']$ quantities given in Table 12. When these are put into the $\langle c'' \rangle$ matrix of Table 7, the entries of Table 13 result; numerical values for ZnO referred to the facet plane (103), are also given.

Table 11
Averaged piezoelectric stress coefficients (C m^{-2}) for class 6*mm*, particularized for ZnO with facet plane (103).

0	0	0	0	$\langle e_{15}'' \rangle$	0		0	0	0	0	−0.155	0
0	0	0	$\langle e_{15}'' \rangle$	0	0	=	0	0	0	−0.155	0	0
$\langle e_{31}'' \rangle$	$\langle e_{31}'' \rangle$	$\langle e_{33}'' \rangle$	0	0	0		−0.185	−0.185	+0.289	0	0	0

Table 12
Resulting elastic stiffnesses from a first rotation of a 6*mm* crystal about its x_1 axis. C and S are cos(θ) and sin(θ), respectively, where θ is the facet angle.

c_{11}'		c_{11}
c_{12}'		$c_{12}C^2 + c_{13}S^2$
c_{13}'		$c_{13}C^2 + c_{12}S^2$
c_{22}'		$c_{11}C^4 + c_{33}S^4 + 2(c_{13} + 2c_{44})C^2S^2$
c_{23}'	=	$c_{13}(C^4 + S^4) + (c_{11} + c_{33} - 4c_{44})C^2S^2$
c_{33}'		$c_{33}C^4 + c_{11}S^4 + 2(c_{13} + 2c_{44})C^2S^2$
c_{44}'		$c_{44}(C^4 + S^4) + (c_{11} + c_{33} - 2c_{13} - 2c_{44})C^2S^2$
c_{55}'		$c_{44}C^2 + c_{66}S^2$
c_{66}'		$c_{66}C^2 + c_{44}S^2$
$(c_{44}' - c_{23}')$		$(c_{44} - c_{23})$

Table 13
Averaged elastic stiffness coefficients (GPa) for class 6*mm*, with numerical values particularized for ZnO with facet plane (103).

$\langle c_{11}'' \rangle$	$\frac{1}{8}[c_{11}(3 + 2C^2) + 3(c_{11}C^4 + c_{33}S^4) + 2(c_{13} + 2c_{44})(1 + 3C^2)S^2]$	205.72
$\langle c_{12}'' \rangle$	$\frac{1}{8}[c_{11}(1 + 6C^2) + (c_{11}C^4 + c_{33}S^4 - 4c_{44}S^4) - 16c_{66}C^2 + 2c_{13}(3 + C^2)S^2]$	117.34
$\langle c_{13}'' \rangle$	$\frac{1}{2}[c_{13}C^2 + c_{13}(C^4 + S^4) + c_{11}(1 + C^2) + (c_{33}C^2 - 4c_{44}C^2 - 2c_{66})S^2]$	111.55
$\langle c_{33}'' \rangle$	$[c_{33}C^4 + c_{11}S^4 + 2(c_{13} + 2c_{44})C^2S^2]$	202.66
$\langle c_{44}'' \rangle$	$\frac{1}{2}[c_{44}C^2 + c_{44}(C^4 + S^4) + c_{66}S^2 + (c_{11} + c_{33} - 2c_{13} - 2c_{44})C^2S^2]$	46.78
$\langle c_{66}'' \rangle$	$\frac{1}{8}[8c_{66}C^2 + (c_{11} + c_{33} - 2c_{13})S^2 + 4c_{44}(1 + C^4)S^2] = (\langle c_{11}'' \rangle - \langle c_{12}'' \rangle)/2$	44.19

4.4. Computation of piezo-coupling values

Piezo-coupling coefficients determine efficacy of piezoelectric transduction. As measures thereof, 'they appear in considerations of bandwidth and insertion loss in transducers and signal processing devices, in the location and spacing of critical frequencies of resonators, and in electrical/mechanical energy conversion efficiency in actuators and energy harvesters' (Ballato & Ballato, 2023). Calculation of these quantities for the one-dimensional case of thickness vibrations of plates and films requires knowledge only of the effective dielectric, piezoelectric, and elastic tensors referred to the plate/film coordinates; these are the $\langle'' \rangle$ quantities in our situation. An eigenvalue equation is solved, yielding three modal elastic stiffnesses, c_m, three modal piezoelectric coefficients, e_m, and the effective permittivity in the thickness direction, ε_3. Then the coupling coefficients are given in the generic form $|k_m| = |e_m|/(c_m\varepsilon_3)^{1/2}$ (Foster *et al.*, 1968; Wittstruck *et al.*, 2005; Ballato & Ballato, 2023).

In Table 14 are given the relevant data for averaged ZnO with zero facet angle. Corresponding wave velocities are $V_m = (c_m/\rho)^{1/2}$. The mass density of bulk crystalline ZnO is $\rho \simeq 5.606$

Table 14
Effective elastic stiffnesses, c_m, piezoelectric coupling coefficients, $|k_m|$, and deviation angles, $|\delta_a|$ of ZnO thin plates or films having tilt (texture) angles $\gamma = 0°(15°)90°$ about an axis lying in the basal plane (001).

Subscript m denotes the wave: a the quasi-longitudinal, and b, c the fast and slow quasi-shears, respectively. Piezo-coupling $|k_c| \equiv 0$. Angle $|\delta_a|$ gives the offset of the a wave motion from the wave progression direction, which is parallel to the plate/film thickness.

Quantity	Unit	$\gamma = 0°$	$\gamma = 15°$	$\gamma = 30°$	$\gamma = 45°$	$\gamma = 60°$	$\gamma = 75°$	$\gamma = 90°$
c_a		228.07	220.11	205.33	201.12	206.64	209.91	210.00
c_b	GPa	42.50	48.36	58.23	57.80	50.14	46.94	47.24
c_c		42.50	42.62	42.95	43.40	43.85	44.18	44.30
$\|k_a\|$	%	27.36	23.16	10.19	6.08	13.66	10.44	0
$\|k_b\|$		0	25.82	37.47	29.93	5.81	20.62	31.66
$\|\delta_a\|$	°	0	3.74	3.28	0.66	1.86	0.74	0

Table 15
The same quantities defined in Table 14, but for ZnO microcrystallites that have undergone the averaging procedure described in the text (see Section 2) to create an engineered crystal with 6*mm* symmetry.

For the entries given, the facet angle for the averaging is that of the (103) plane, ($\theta \simeq 31.664°$). The engineered crystal is then tilted by angles $\gamma = 0°(15°)90°$ about an axis lying in its basal plane (001), *i.e.* the plane of the substrate, as a basis for comparison with the entries in Table 14, but more importantly, to suggest that untextured, engineered, crystals may be created to meet desired design criteria

Quantity	Unit	$\gamma = 0°$	$\gamma = 15°$	$\gamma = 30°$	$\gamma = 45°$	$\gamma = 60°$	$\gamma = 75°$	$\gamma = 90°$
c_a		203.74	203.66	203.86	204.73	205.60	205.81	205.72
c_b	GPa	46.78	46.96	47.05	46.69	46.45	46.80	47.11
c_c		46.78	46.61	46.13	45.48	44.84	44.36	44.19
$\|k_a\|$	%	7.29	5.76	2.01	1.89	3.82	2.93	0
$\|k_b\|$		0	7.87	11.44	8.89	1.86	5.32	8.30
$\|\delta_a\|$	°	0	0.05	0.23	0.34	0.19	0.01	0

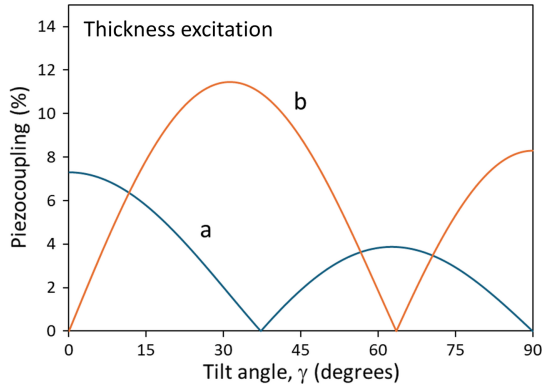

Figure 2
Piezo-couplings $|k_a|$ and $|k_b|$ of an engineered ZnO plate formed by averaging over facet angle $\theta \simeq 31.664°$, plotted versus tilt (texture) angle γ. Driving electric field is normal to the substrate plane. Waves a and b are quasi-thickness extension, and quasi-thickness shear, respectively. Note the similar, but reduced, values of coupling compared with Foster *et al.* (1968), where the facet angle $\theta = 0°$. Wave c, (pure shear) is inert to thickness-directed fields. In devices using the quasi-shear mode, a practical tilt angle would be at, or near, the value where $|k_a| = 0$; here the b wave coupling is nearly a maximum.

$\times 10^3$ (kg m^{-3}) (Pearton *et al.*, 2005). Table 15 provides this data for averaged ZnO with facet angle of the (103) plane. The $|k_m|$ values are plotted in Fig. 2, as a function of tilt angle γ, for averaged ZnO with facet angle of the (103) plane.

5. Conclusions

The rotating substrate method of crystallite deposition is modeled, allowing computation of effective material coefficients of the layers resulting from the averaging. Modeling of the averaging applies generally to tensors of any rank, but is applied here to dielectric, piezoelectric, and elastic coefficients. A worked numerical example particularized to 6*mm* ZnO is provided. Layers comprised of crystallites deposited with zero facet angle are contrasted with those deposited on facet plane (103). It is proposed that the method enables creation of 'engineered' layered structures.

Acknowledgements

JB acknowledges support from the J. E. Sirrine Foundation.

References

Akçakaya, E., Farnell, G. W. & Adler, E. L. (1990). *J. Appl. Phys.* **68**, 1009–1012.
Auger, M. A., Gago, R., Fernández, M., Sánchez, O. & Albella, J. M. (2002). *Surf. Coat. Technol.* **157**, 26–33.
Ballato, A. & Ballato, J. (2023). *Int. J. Ceram. Eng. Sci.* **5**, e10182.
Bechmann, R. (1960). *Acta Cryst.* **13**, 110–113.
Bechmann, R. & Hearmon, R. F. S. (1969). *The Third Order Elastic Constants*. In *Landolt-Börnstein – Numerical Data and Functional Relationships. Group III*, Vol. 2. Berlin: Springer.
Behrisch, R. (2013*a*). Sputtering by Particle Bombardment I: Physical Sputtering of Single-Element Solids. Berlin, Heidelberg: Springer.
Behrisch, R. (2013*b*). *Sputtering by Particle Bombardment II: Sputtering of Alloys and compounds, Electron and Neutron Sputtering, Surface Topography.* Berlin, Heidelberg: Springer.
Bhagavantam, S. & Suryanarayana, D. (1949). *Acta Cryst.* **2**, 21–26.
Bjurström, J., Wingqvist, G. & Katardjiev, I. (2006). *IEEE Trans. Ultrason. Ferroelect. Freq. Contr.* **53**, 2095–2100.
Bond, W. L. (1943). *Bell Syst. Tech. J.* **22**, 1–72.
Brendel, R. (1979). *Acta Cryst.* A**35**, 525–533.
Bundesmann, C. & Neumann, H. (2018). *J. Appl. Phys.* **124**, 231102.
Bunge, H.-J. (1982). *Texture Analysis in Materials Science: Mathematical Methods*. London: Butterworths.
Bykhovski, A. D., Gelmont, B. L. & Shur, M. S. (1997). *J. Appl. Phys.* **81**, 6332–6338.
Cady, W. G. (1946). *Piezoelectricity: An Introduction to the Theory, Applications of Electromechanical Phenomena in Crystals*. New York: McGraw-Hill.
Cady, W. G. (1964). *Piezoelectricity: An Introduction to the Theory, Applications of Electromechanical Phenomena in Crystals.* New York: Dover.
Clement, M., Olivares, J., Capilla, J., Sangrador, J. & Iborra, E. (2012). *IEEE Trans. Ultrason. Ferroelect. Freq. Contr.* **59**, 128–134.
Dean, C. R., Wang, L., Maher, P., Forsythe, C., Ghahari, F., Gao, Y., Katoch, J., Ishigami, M., Moon, P., Koshino, M., Taniguchi, T., Watanabe, K., Shepard, K. L., Hone, J. & Kim, P. (2013). *Nature*, **497**, 598–602.
Du, J., Xian, K., Wang, J. & Yang, J. (2009). *Ultrasonics*, **49**, 149–152.
Dvoesherstov, M. Yu., Cherednik, V. I., Bosov, S. I., Orlov, I. Ya. & Rudenko, O. V. (2013). *Acoust. Phys.* **59**, 513–520.
Fieschi, R. (1957). *Physica*, **23**, 972–976.
Foster, N. F., Coquin, G. A., Rozgonyi, G. A. & Vannatta, F. A. (1968). *IEEE Trans. Sonics Ultrason.* **15**, 28–40.
Fumi, F. G. (1952*a*). *Acta Cryst.* **5**, 44–48.
Fumi, F. G. (1952*b*). *Acta Cryst.* **5**, 691–694.
Fumi, F. G. (1952*c*). *Nuovo Cimento*, **9**, 739–756.
Hearmon, R. F. S. (1957). *Acta Cryst.* **10**, 121–124.
Iborra, E., Clement, M., Capilla, J., Olivares, J. & Felmetsger, V. (2012). *Thin Solid Films*, **520**, 3060–3063.
Institute of Radio Engineers Standards Committee (1949). *Proc. IRE* **37**, 1378–1395.
Jaffe, H. & Berlincourt, D. A. (1965). *Proc. IEEE*, **53**, 1372–1386.
Juretschke, H. J. (1952). *Acta Cryst.* **5**, 148–149.
Kushibiki, J.-I., Ohashi, Y., Arakawa, M. & Tanaka, T. (2009). *J. Appl. Phys.* **105**, 114913.
Lakin, K. M. (2003). *IEEE Microw.* **4**, 61–67.
Li, Y., Liu, X., Wen, D., Lv, K., Zhou, G., Zhao, Y., Xu, C. & Wang, J. (2020). *Acta Cryst.* B**76**, 233–240.
Link, M., Schreiter, M., Weber, J., Primig, R., Pitzer, D. & Gabl, R. (2006). *IEEE Trans. Ultrason. Ferroelect. Freq. Contr.* **53**, 492–496.
MacDonald, A. H. (1988). *Fibonacci Superlattices*, edited by C. R. Leavens & R. Taylor, pp. 347–380. In *Interfaces, Quantum Wells, and Superlattices*, NATO ASI Series, Vol. 179. Boston, MA: Springer.
Martin, P. M. (2010). *Handbook of Deposition Technologies for Films and Coatings*, edited by P. M. Martin, pp. 1–31. Amsterdam: Elsevier.
Mason, W. P. (1966). *Crystal Physics of Interaction Processes*. New York: Academic.
Mertin, S., Heinz, B., Rattunde, O., Christmann, G., Dubois, M.-A., Nicolay, S. & Muralt, P. (2018). *Surf. Coat. Technol.* **343**, 2–6.
Moreria, M., Bjurström, J., Kubart, T., Kuzavas, B. & Katardjiev, I. (2011). *IEEE Ultrason. Symp. Proc.* pp. 1238–1241.
Mouldi, A. & Kanzari, M. (2013). *PIER M*, **32**, 169–180.
Newell, W. E. (1964). *Proc. IEEE*, **52**, 1603–1608.
Nguyen, N., Johannessen, A., Rooth, S. & Hanke, U. (2019). *Ultrasonics*, **94**, 92–101.
Noh, Y.-K., Park, C.-H., Oh, J.-E., Lee, S.-T. & Kim, M.-D. (2014). *J. Korean Phys. Soc.* **64**, 1577–1580.
Nye, J. F. (1985). *Physical Properties of Crystals: Their Representation by Tensors and Matrices*. Oxford University Press.
Pearton, S. J., Norton, D. P., Ip, K., Heo, Y. W. & Steiner, T. (2005). *Prog. Mater. Sci.* **50**, 293–340.
Schuller, I. K. (1980). *Phys. Rev. Lett.* **44**, 1597–1600.
Stedile, F. C., Freire, F. L. Jr, Schreiner, W. H. & Baumvol, I. J. R. (1994). *Vacuum*, **45**, 441–446.
Suwas, S. & Gurao, N. P. (2008). *J. Indian Inst. Sci.* **88**, 151–177.
Wittstruck, R. H., Emanetoglu, N. W., Lu, Y., Laffey, S. & Ballato, A. (2005). *J. Acoust. Soc. Am.* **118**, 1414–1423.
Yanagitani, T., Kiuchi, M., Matsukawa, M. & Watanabe, Y. (2007*a*). *J. Appl. Phys.* **102**, 024110.